Carrier transport in broken-gap heterostructures tuned by a magnetic field

K. Nilsson,[1] A. Zakharova,[2] I. Semenikhin,[2] and K. A. Chao[1]
[1]*Department of Physics, Lund University, Sölvegatan 14A, S223 62 Lund, Sweden*
[2]*Institute of Physics and Technology of the Russian Academy of Sciences, Nakhimovskii Avenue 34, Moscow 117218, Russia*
(Received 13 November 2006; revised manuscript received 19 February 2007; published 14 May 2007)

We have performed an eight-band $\mathbf{k}\cdot\mathbf{p}$ model calculation on the current-voltage (*I-V*) curves associated with interband magnetotransport in a double-barrier broken-gap heterostructure using the Burt-Foreman multiband envelope function theory and the scattering matrix approach. In a sample with very thin barriers, the broadening Γ_0 of a virtual bound state with energy E_0 can be very large. Depending on the relative values of Γ_0 and $|E_0 - E_F|$, where E_F is the Fermi energy, the behavior of the *I-V* curve can be either of Ohmic type or of resonant-tunneling type, and can be tuned from one to the other by changing the applied magnetic-field strength.

DOI: 10.1103/PhysRevB.75.205318 PACS number(s): 73.21.Ac, 73.40.Kp, 73.40.Gk

I. INTRODUCTION

Understanding the electronic properties of broken-gap heterostructures has been a great challenge for fundamental research because of the overlap between the conduction band of one material component and the valence band of the other component. Since the proposal of Yang *et al.*[1] to use such heterostructures for fabricating interband cascade lasers, there have been many works on practical engineering designs.[2–4] The energy range of the band overlap is very small, typically of the order 150–200 meV. Therefore, very accurate calculations of energy-level structures in the band-overlap region is one of the most important tasks, especially for the interpretation of experimental data and for the performance of high-power interband cascade lasers. In this respect, the relevant subsystem is the InAs/GaSb quantum well which exhibits enormous complexity due to the spin-orbit interaction, the bulk anisotropy, and the lattice-mismatch induced strain, not to mention the effect of an external magnetic field.

The outcome of a theoretical study on broken-gap heterostructures is thus very sensitive to the choice of model Hamiltonian. The accumulated knowledge in the past has made it clear that for reliable results, one needs a model Hamiltonian with eight bands. Electronic energy-level structures in InAs/GaSb quantum wells and the multiple anticrossings resulting from hybridization between electrons, light holes, and heavy holes were studied using an eight-band Hamiltonian, first without considering the lattice-mismatch induced strain[5–8] and later with the strain included.[9,10] The degeneracy of each energy level in the band-overlap region at the Γ point is lifted by an applied magnetic field. The level splittings can be as large as about 20 meV at a magnetic-field strength of 2 T, which is significant because the band overlap itself is only about 150–200 meV. Investigations of Landau-level structures are further complicated by the electron-hole hybridization, by which the conventional Landau-level index is no longer a good quantum number. With an external magnetic field applied parallel to the growth direction, Landau-level structures in the broken-gap quantum wells were first studied with a six-band model[11,12] and later with an eight-band model.[13,14] Knowing the energy-level structures, one can analyze the effective g factors[12,13] and cyclotron masses[11,13] of the electron-hole gas. These two physical quantities are very sensitive to the small separation of the relevant energy levels, and consequently charge accumulation and band-bending effects must be taken into account.[5,15] Very recently, the required accurate eight-band $\mathbf{k}\cdot\mathbf{p}$ model calculations for broken-gap systems under an external magnetic field have emerged with a partially self-consistent scheme.[13]

To understand carrier transport in broken-gap heterostructures along the direction perpendicular to the interfaces,[16–19] which is basically of interband-tunneling nature, we also need to derive accurate electronic energy levels. The relevant systems are double-barrier broken-gap structures with typical band diagrams as the one shown in Fig. 1. Carriers move from the InAs source at the left into the InAs drain at the right through the hybridized energy levels in the InAs/GaSb quantum well. The understanding of transport phenomena has improved progressively in the past, starting from simple model calculations. It was well known that in the absence of an external magnetic field, at the in-plane wave vector $\mathbf{k}_{\parallel}=0$, the electron states and the heavy-hole states are essen-

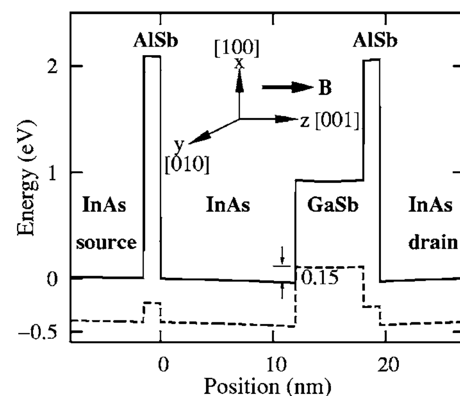

FIG. 1. The self-consistently calculated band diagram of the InAs/AlSb/InAs/GaSb/AlSb/InAs double-barrier broken-gap heterostructure, with a 12 nm InAs layer and a 6 nm GaSb layer in the well. The solid curve is the conduction band and the dashed curve the valence band. The coordinate system and magnetic-field direction are also shown.

 ©2007 The American Physical Society

tially decoupled, since the very weak coupling caused by the low C_{2v} interface symmetry can be neglected. Consequently, the heavy-hole states in the well do not contribute to the interband-tunneling current. For $\mathbf{k}_{\parallel} \neq 0$ and/or nonzero magnetic field, electron, light-hole, and heavy-hole states can hybridize considerably,[8,10–13] and so the heavy-hole-like states can contribute to interband tunneling as much as the light-hole-like states.[20–23] An eight-band $\mathbf{k}\cdot\mathbf{p}$ Hamiltonian, including strain and bulk anisotropy but not an applied magnetic field, was used to investigate transmission coefficients and current-voltage $(I\text{-}V)$ characteristics.[22] To pinpoint the effect of a magnetic field on interband tunneling, a simple six-band model calculation, without strain and bulk anisotropy, discovered that due to band-state mixing, tunneling processes that do not conserve the Landau-level index give non-negligible contributions to the current.[24] Strain and bulk anisotropy were later included, and spin-dependent magnetotunneling was examined.[25] While in all the above-mentioned works the magnetic field is applied along the growth direction, the eight-band model has also been used to investigate magnetotunneling with the magnetic field perpendicular to the growth direction.[26]

After the demonstration of the importance of including charge transfer in Landau-level-structure calculations,[13] a similar partially self-consistent calculation of interband magnetotunneling through these Landau levels naturally follows. However, the partially self-consistent study performed in the present paper is not only for achieving quantitative accuracy alone but also for investigating novel phenomena. When changing the magnetic field, all Landau levels in the quantum well change continuously, and one by one the levels intersect the Fermi level E_F. If the barriers in the double-barrier tunneling structure are sufficiently thin, there are virtual bound states $E_l+i\Gamma_l$ in the quantum well with a large broadening Γ_l. By tuning the magnetic field, we can move one energy E_l very close to E_F, such that the separation between E_l and E_F becomes comparable to Γ_l. In this case, the interband tunneling occurs without a bias threshold. In other words, the carrier transport exhibits an Ohmic behavior instead of a resonant-tunneling behavior with a finite bias threshold. Consequently, with an applied magnetic field, we can tune the resonant-tunneling transport into Ohmic transport and vice versa. It is important to point out that this fundamental phenomenon is intrinsic to the broken-gap systems with narrow barriers and can be demonstrated with our partially self-consistent calculations. The analytical works which lead to this final result can be found in several published papers cited above, and we will only outline the analysis in Sec. II. The electric current and its Ohmic behavior will be illustrated in Secs. III and IV, respectively. The impact of our finding on the interpretation of relevant experiments will be discussed in Sec. V.

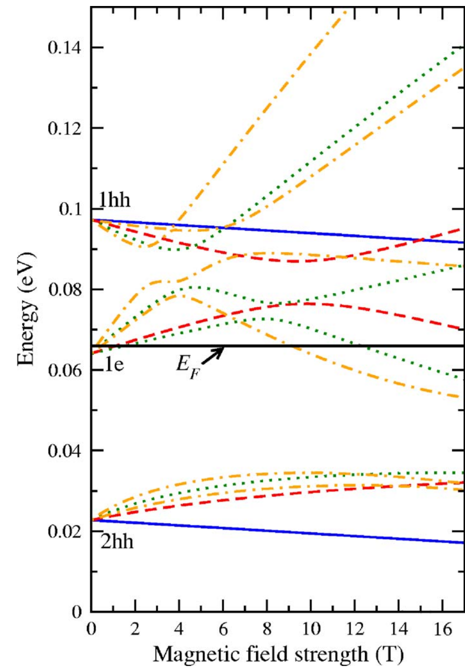

FIG. 2. (Color online) Landau levels in the band-overlap energy region for the sample structure in Fig. 1. The solid curves show levels with $n=-2$, dashed curves $n=-1$, dotted curves $n=0$, and dashed-dotted curves $n=1$. The Fermi energy level E_F at 66 meV is marked as the thick solid line.

II. OUTLINE OF ANALYSIS

Broken-gap heterostructures have been extensively investigated using the $\mathbf{k}\cdot\mathbf{p}$ Hamiltonian, either with a six-band model or with an eight-band model. Depending on the degree of sophistication, the model Hamiltonian sometimes includes the lattice-mismatch induced strain and/or bulk anisotropy. To compare with the results of different types of experiments, terms representing the effects of electric and/or magnetic field may be included in the model. The Hamiltonian is, in general, rather complicated and is often simplified with either the spherical or the axial approximation when solving the Schrödinger equation. In the absence of an external magnetic field, self-consistent calculations have been performed to investigate the characteristic properties of the electron-hole gas in broken-gap systems. In the present work, we will use the eight-band $\mathbf{k}\cdot\mathbf{p}$ Hamiltonian $\hat{H}_8$ including the lattice-mismatch induced strain, the bulk anisotropy, as well as the spin-orbit interaction for a system with a magnetic field applied parallel to the growth direction. The charge accumulation in the system is also taken into account to provide self-consistent results for zero magnetic field and sufficiently accurate partially self-consistent results for finite magnetic field. The essential parts of this model Hamiltonian and associated computation scheme are given in Refs. 13 and 22. Here, we will only outline the theoretical analysis, and the reader is suggested to refer to Refs. 13 and 22 for details.

The eight-band $\mathbf{k}\cdot\mathbf{p}$ Burt-Foreman Hamiltonian[27] for the Γ point in a zinc-blende crystal can be separated into three parts as

$$\hat{H}_8 = \hat{H}_k + \hat{H}_\varepsilon + \hat{H}_Z, \tag{1}$$

where $\hat{H}_k$ includes the $\mathbf{k}$-dependent part and the spin-orbit interaction, $\hat{H}_\varepsilon$ represents the effect of strain on the energy

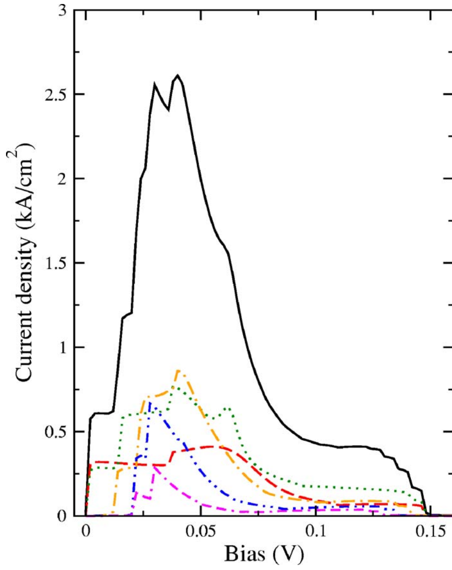

FIG. 3. (Color online) *I-V* characteristics of the broken-gap structure specified in Fig. 1. The magnetic field is 2 T. The solid curve is the total current, and the other curves show the partial nonvanishing contributions from states with different n; the dashed curve is for $n=-1$, the dotted curve for $n=0$, the dashed-dotted curve for $n=1$, the dashed-dotted-dotted curve for $n=2$, and the dashed-dashed-dotted curve is for $n=3$.

levels, and $\hat{H}_Z$ is the Zeeman interaction term. The explicit form of all elements of the matrix operators

$$\hat{H}_k = \begin{pmatrix} \hat{H}_{-+} & \hat{H}_{--} \\ \hat{H}_{++} & \hat{H}_{+-} \end{pmatrix}, \tag{2}$$

$$\hat{H}_\varepsilon = \begin{pmatrix} \hat{H}_{\varepsilon,4} & 0 \\ 0 & \hat{H}_{\varepsilon,4} \end{pmatrix}, \tag{3}$$

$$\hat{H}_Z = \begin{pmatrix} \hat{H}_{Z,4} & 0 \\ 0 & -\hat{H}_{Z,4} \end{pmatrix} \tag{4}$$

are given in Ref. 13, together with the justification for the neglect of small terms. The Hamiltonian in Ref. 13 is suitable for calculating the static properties but not for the transport processes which we will investigate here using the scattering matrix method.[27,28] To study carrier transport, we need to slightly modify the partial Hamiltonian $\hat{H}_k$ in order to avoid spurious solutions. First, we follow the argument of Foreman[29] and set the quantity A_c in $\hat{H}_k$ to zero. This quantity represents the effect of remote bands on the electron effective mass. As a consequence, the energy E_P, which appears through the interband momentum matrix element P, is changed to $E_P=(3m_0/m_c)[2/E_g+1/(E_g+\Delta)]^{-1}$, where m_0 is the free electron mass, m_c the conduction-band effective mass, E_g the band gap, and Δ the split-off energy. In this way, the two conduction-band envelope functions Ψ_1 and Ψ_5 are determined from the six valence-band envelope functions Ψ_2, Ψ_3, Ψ_4, Ψ_6, Ψ_7, and Ψ_8 as

$$\Psi_1 = (E-E_c-a_c\varepsilon)^{-1}P\left[\sqrt{\frac{2}{3}}i\hat{K}_z\Psi_2 - \sqrt{\frac{1}{3}}i\hat{K}_z\Psi_3 + \hat{K}_+\Psi_4 + \sqrt{\frac{1}{3}}\hat{K}_-\Psi_6 + \sqrt{\frac{2}{3}}\hat{K}_-\Psi_7\right], \tag{5}$$

$$\Psi_5 = (E-E_c-a_c\varepsilon)^{-1}P\left[\sqrt{\frac{1}{3}}\hat{K}_+\Psi_2 + \sqrt{\frac{2}{3}}\hat{K}_+\Psi_3 + \sqrt{\frac{2}{3}}i\hat{K}_z\Psi_6 - \sqrt{\frac{1}{3}}i\hat{K}_z\Psi_7 - \hat{K}_-\Psi_8\right]. \tag{6}$$

Here, E is the carrier energy, E_c the conduction-band edge, a_c the conduction-band deformation potential, ε the trace of the strain tensor, and $\hat{K}_z=\hat{k}_z$. The momentum operators $\hat{K}_x=\hat{k}_x$ and $\hat{K}_y=\hat{k}_y+xes/\hbar$ in the presence of a magnetic field $\mathbf{B}=(0,0,z)$, with $s=eB/\hbar$, are rearranged as $\hat{K}_\pm = \mp i(\hat{K}_x \pm i\hat{K}_y)/\sqrt{2}$.

The eight coupled differential equations in the Schrödinger equation $\hat{H}_8\Psi=E\Psi$ can now be rearranged into a set of six coupled equations

$$\hat{H}_6\Psi = E\Psi, \tag{7}$$

with $\Psi=[\Psi_2\Psi_3\Psi_4\Psi_6\Psi_7\Psi_8]^T$. The 6×6 matrix operator $\hat{H}_6$ is easily constructed from $\hat{H}_8$ by deleting the conduction-band rows and columns, replacing the modified Luttinger parameters γ_1, γ_2, and γ_3 with $\gamma_1'=\gamma_1-E_P/[3(E-E_c-a_c\varepsilon)]$ and $\gamma_{2,3}'=\gamma_{2,3}-E_P/[6(E-E_c-a_c\varepsilon)]$, and removing the small elements $\hat{H}_{Z_{11}}$ and $\hat{H}_{Z_{55}}$.

We solve the Schrödinger equation [Eq. (7)] together with the Poisson equation, as in Ref. 13. In the absence of an applied magnetic field, we perform a complete self-consistent calculation to find the self-consistent potential V_s and the change N_0 of the carrier concentration in the well. We then turn on the magnetic field $\mathbf{B}$ and use V_s to derive the eigensolutions which we use to calculate the additional change of the quantum-well carrier concentration N_B. For magnetic-field strengths up to 10 T, we found that N_B is much smaller than N_0 such that the ratio N_B/N_0 is less than 0.05. Consequently, under an applied magnetic field, the self-consistent correction to the potential V_s is less than 5%. This theoretical conclusion agrees with the experimental finding of Barnes *et al.* in Ref. 30 where the carrier density in InAs/GaSb and InAs/GaInSb superlattices under an applied magnetic field was derived. As shown in Fig. 4 of Ref. 30, the two-dimensional carrier density is almost the same at zero field as at a high field of about 40 T.

In the absence of a magnetic field, for samples with a narrow well (of the order 20 nm) and thin barriers (of the order 2 nm), we found that the self-consistent corrections to the energy levels are of the order of 5 meV. Therefore, when an external field is applied, the additional self-consistent correction to each energy level is less than 0.25 meV, and the effect on the transport phenomena, to be investigated in the later part of this paper, is negligibly small. At the same time, a complete self-consistent calculation at a finite magnetic

field is extremely time consuming not only because a large number of occupied Landau levels must be considered but also due to the current continuity condition as explained in Ref. 31. In our numerical calculations, we will therefore use V_s also for finite magnetic fields. We call this computation scheme partially self-consistent.

Since our interest is to study the dynamical processes in the band-overlap energy region, the difference between the chemical potential in the source and in the drain should not be larger than this overlap. The applied bias is therefore less than 0.2 V. For samples with a thin well and thin barriers, which are the ones we study here, the bias-induced change of the charge redistribution in the well is also negligibly small. Therefore, we can derive sufficiently accurate results using the partially self-consistent scheme at finite magnetic field and finite bias.

We divide the heterostructure into N sublayers such that sublayer 1 is in the source just before the left barrier and sublayer N is in the drain just behind the right barrier. The $N-2$ sublayers in the active region (well and barriers) are of equal width. In each sublayer, the self-consistently calculated band edges are approximated with constants. The envelope function $\psi_{\alpha}^{(j)}$ of the bulk state α in sublayer j can be expressed as[32]

$$\psi_{\alpha}^{(j)} = \mathbf{h}_{\alpha}^{(j)} \exp(ik_y y + ik_z z), \tag{8}$$

with

$$\mathbf{h}^{(j)} = \begin{pmatrix} C_1 F_n(x') \\ C_2 F_n(x') \\ C_3 F_n(x') \\ C_4 F_{n-1}(x') \\ C_5 F_{n+1}(x') \\ C_6 F_{n+1}(x') \\ C_7 F_{n+1}(x') \\ C_8 F_{n+2}(x') \end{pmatrix}, \tag{9}$$

where $F_{\nu}(x')$ is the normalized harmonic oscillator function with Landau-level quantum number ν and $x'=x+k_y/s$. Here, the warping terms in the Hamiltonian are neglected and we solve the Schrödinger equation for each quantum number $n=-2,-1,0,\ldots$, separately. After removing the first and fifth elements in $\mathbf{h}^{(j)}$, we substitute $\psi_{\alpha}^{(j)}$ into the Schrödinger equation [Eq. (7)] to find[32]

$$\begin{pmatrix} \mathbf{0} & \mathbf{1} \\ -(H^{(2)})^{-1}H^{(0)} & -(H^{(2)})^{-1}H^{(1)} \end{pmatrix} \begin{pmatrix} \mathbf{e}^{(j)} \\ k_z \mathbf{e}^{(j)} \end{pmatrix} = k_z \begin{pmatrix} \mathbf{e}^{(j)} \\ k_z \mathbf{e}^{(j)} \end{pmatrix}, \tag{10}$$

where $\mathbf{e}^{(j)}=[C_2C_3C_4C_6C_7C_8]^T$. The explicit expressions for the Hermitian matrices $H^{(0)}$, $H^{(1)}$, and $H^{(2)}$ are given in Table I. The size of each matrix, μ, depends on n. The relationship is $\mu=1,3,5$ for $n=-2,-1,0$ and $\mu=6$ for $n\geqslant 1$.

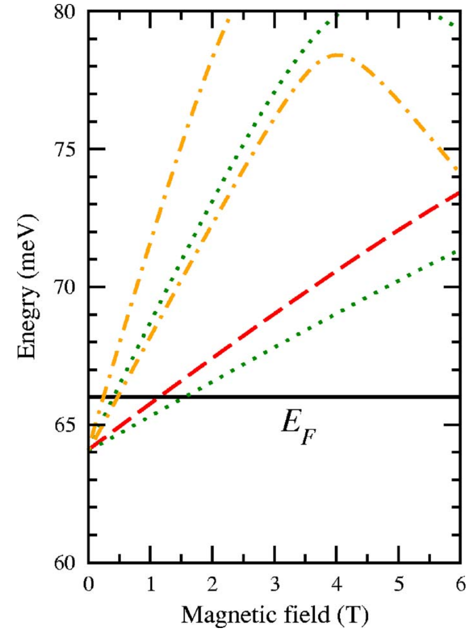

FIG. 4. (Color online) Magnified part of Fig. 2 showing the low-magnetic-field Landau levels close to the Fermi level E_F.

The envelope function $\Psi^{(j)}$ in the jth sublayer is constructed from the 2μ solutions $k_{z,\alpha}^{(j)}$ of Eq. (10) and the corresponding vectors $\mathbf{h}_{+\alpha}^{(j)}$ with coefficients $a_{\alpha}^{(j)}$ for the forward bulk states, but $\mathbf{h}_{-\alpha}^{(j)}$ with coefficients $b_{\alpha}^{(j)}$ for the backward bulk states

$$\Psi^{(j)} = \exp(ik_y y)\sum_{\alpha=1}^{\mu} \{a_{\alpha}^{(j)} \exp[ik_{z,\alpha}^{(j)}(z-z_{j-1})]\mathbf{h}_{+\alpha}^{(j)} + b_{\alpha}^{(j)} \exp[-ik_{z,\alpha}^{(j)}(z-z_j)]\mathbf{h}_{-\alpha}^{(j)}\}. \tag{11}$$

When matching the solutions of the adjacent sublayers, the continuity condition is imposed only on the valence-band components of the envelope function, because, as pointed out in Ref. 29, the conduction-band envelope functions are discontinuous when the quantity A_c is set to zero. The second matching condition is the continuity of the probability current density derived by integrating Eq. (7) across an interface.

In the following sections, we will discuss carrier transport in the broken-gap tunneling structure shown in Fig. 1. The thin well of this sample consists of a 12 nm InAs layer and a 6 nm GaSb layer. The thickness of each AlSb barrier is only 1.5 nm. The substrate is InAs and the donor concentration in the n-doped contacts is 2×10^{17} cm^{-3}. Using the basis-expansion computation scheme given in Ref. 13, we have calculated the energy levels in the quantum well shown in Fig. 1 partially self-consistently. The energy levels in the band-overlap energy region are shown in Fig. 2 as functions of the magnetic field. The levels are labeled according to their primary characters at zero magnetic field: e for electronlike and hh for heavy-hole-like. We will also use lh for light-hole-like. Solid curves are for levels with $n=-2$, dashed curves for $n=-1$, dotted curves for $n=0$, and dashed-dotted curves for $n=1$. For clarity, levels with higher values

TABLE I. Explicit expressions for the elements in the upper triangles of the Hermitian matrices $H^{(2)}$, $H^{(1)}$, and $H^{(0)}$. The following notations are used: $E'=E-E_v$, $S_1=[a_v-(b/2)]2\varepsilon_{xx}+(a_v+b)\varepsilon_{zz}$, $S_2=\sqrt{2}b(\varepsilon_{xx}-\varepsilon_{zz})$, $S_3=a_v(2\varepsilon_{xx}+\varepsilon_{zz})$, $S_4=[a_v+(b/2)]2\varepsilon_{xx}+(a_v-b)\varepsilon_{zz}$, $\gamma_N=2\gamma_1'-4\gamma_2'-6\gamma_3'+2$, and $\gamma_s=\gamma_2'+\gamma_3'$, where E_v is the valence-band edge; a_v, b, and d the valence-band deformation potentials, ε_{ii} strain tensor components; and μ_B is the Bohr magneton.

$H_{11}^{(2)}=H_{44}^{(2)}=-\gamma_1'-2\gamma_2'$	$H_{12}^{(2)}=H_{45}^{(2)}=2\sqrt{2}\gamma_2'$
$H_{22}^{(2)}=H_{55}^{(2)}=-\gamma_1'$	$H_{33}^{(2)}=H_{66}^{(2)}=-\gamma_1'+2\gamma_2'$
$H_{13}^{(1)}=-\sqrt{2}H_{23}^{(1)}=i\gamma_3'\sqrt{24sn}$	$H_{46}^{(1)}=-\sqrt{2}H_{56}^{(1)}=-i\gamma_3'\sqrt{24s(n+2)}$
$H_{15}^{(1)}=-H_{24}^{(1)}=6i\gamma_3'\sqrt{s(n+1)}$	
$H_{11}^{(0)}=s(\gamma_2'-\gamma_1')(2n+1)+s\gamma_N/6+\frac{2m_0}{\hbar^2}(S_{11}^{+}-E')$	
$H_{22}^{(0)}=-s\gamma_1'(2n+1)+s\gamma_N/3+\frac{2m_0}{\hbar^2}(S_{22}^{+}-E')$	
$H_{33}^{(0)}=-s(\gamma_1'+\gamma_2')(2n-1)+s\gamma_N/2+\frac{2m_0}{\hbar^2}(S_{33}^{+}-E')$	
$H_{44}^{(0)}=s(\gamma_2'-\gamma_1')(2n+3)-s\gamma_N/6+\frac{2m_0}{\hbar^2}(S_{11}^{-}-E')$	
$H_{55}^{(0)}=-s\gamma_1'(2n+3)-s\gamma_N/3+\frac{2m_0}{\hbar^2}(S_{22}^{-}-E')$	
$H_{66}^{(0)}=-s(\gamma_1'+\gamma_2')(2n+5)-s\gamma_N/2+\frac{2m_0}{\hbar^2}(S_{33}^{-}-E')$	
$H_{12}^{(0)}=-s\sqrt{2}\gamma_2'(2n+1)+s\gamma_N/(3\sqrt{2})+\frac{2m_0}{\hbar^2}S_{12}^{+}$	
$H_{45}^{(0)}=-s\sqrt{2}\gamma_2'(2n+3)-s\gamma_N/(3\sqrt{2})+\frac{2m_0}{\hbar^2}S_{12}^{-}$	
$H_{26}^{(0)}=\sqrt{2}H_{16}^{(0)}=s\sqrt{6(n+2)(n+1)}\gamma_s$	$H_{35}^{(0)}=\sqrt{2}H_{34}^{(0)}=-s\sqrt{6(n+1)n}\gamma_s$
$S_{11}^{\pm}=S_1\pm\mu_B B/3$	$S_{12}^{\pm}=S_2\mp 2\sqrt{2}\mu_B B/3$
$S_{22}^{\pm}=S_3-\Delta\mp\mu_B B/3$	$S_{33}^{\pm}=S_4\pm\mu_B B$

of n are excluded from the figure. The Fermi energy $E_F=66$ meV is marked as the black horizontal line.

This type of energy-level structures for different sample structures were presented in Ref. 13, where the cyclotron masses and effective g factors in the anticrossing region were discussed in detail. In the present work, we will pay attention to the energy region in the vicinity of the Fermi energy, which is relevant to the transport properties. As can be seen in Fig. 2, with increasing magnetic field, the Fermi energy intersects various energy levels. Since the sample in Fig. 1 has very thin barriers, each energy level is broadened significantly. Therefore, the carrier transport may exhibit interesting behavior close to each intersecting point. This will be investigated in the following sections.

III. ELECTRIC CURRENT

The matching conditions between the jth and the $(j+1)$th sublayers provide equations that connect the coefficients $a_\alpha^{(j)}$ and $a_\alpha^{(j+1)}$ of the forward states and the coefficients $b_\alpha^{(j)}$ and $b_\alpha^{(j+1)}$ of the backward states. Using the scattering matrix technique[28] together with appropriate initial conditions, all these coefficients can be determined. To calculate the transmission coefficient $T_{ti}(E)$ for interband tunneling from the state i in the source $(j=1)$ to the state t in the drain $(j=N)$, we should set $\mathbf{b}^{(N)}=0$ and $a_\alpha^{(1)}=\delta_{i\alpha}$.

The probability current densities j are calculated from the current-density operator $\hat{j}_z=\frac{i}{\hbar}[\hat{H}_8,z]$ as

$$j=\mathrm{Re}(\Psi^\dagger\hat{j}_z\Psi), \tag{12}$$

with the appropriate envelope function Ψ from Eq. (11). To calculate the incident probability current densities j_i, we should only keep the forward states in the source, and for the transmitted probability current densities j_t, only the forward states in the drain should be retained. Knowing j_i and j_t, the transmission coefficient $T_{ti}(E)$ is readily obtain as

$$T_{ti}(E)=\left(\int dx j_t\right)\Big/\left(\int dx j_i\right). \tag{13}$$

In terms of the transmission coefficients and the Fermi-Dirac distribution $f(E)$, the electric current density $I(V_b)$ under an applied positive bias V_b is calculated as

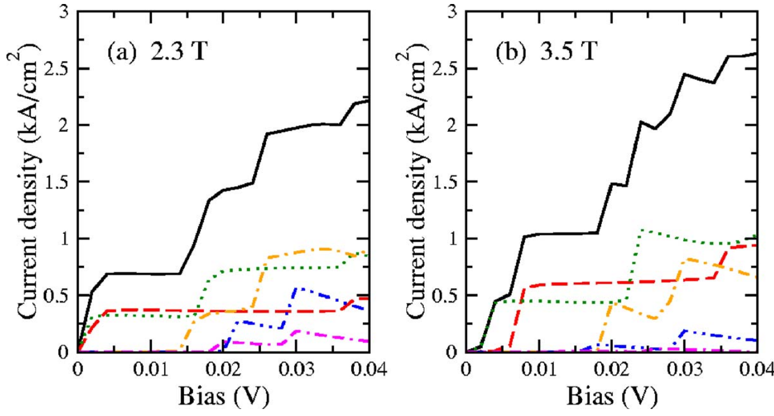

FIG. 5. (Color online) Low-bias *I*-*V* characteristics of the broken-gap structure specified in Fig. 1 for (a) $B=2.3$ T and (b) $B=3.5$ T.

$$I(V_b) = \sum_{ti} I_{ti}(V_b) = \sum_{ti} \frac{es}{(2\pi)^2\hbar} \int dE T_{ti}(E)[f(E) - f(E + eV_b)]. \tag{14}$$

To calculate the *I*-*V* curve for the sample specified in Fig. 1, we have taken the lattice constants, the deformation potentials, and the stiffness constants from Ref. 33 and all other material parameters from Ref. 7. Since almost all relevant energies appearing in the problem discussed here are of the order a few meV, for practical purposes, we set the temperature to zero in our calculations. The so-obtained *I*-*V* characteristics for an applied magnetic field of 2 T is shown in Fig. 3. The solid curve is the total current density, while the other curves represent the partial current densities contributed from states with different n; the dashed curve is for $n=-1$, the dotted curve for $n=0$, the dashed-dotted curve for $n=1$, the dashed-dotted-dotted curve for $n=2$, and the dashed-dashed-dotted curve is for $n=3$. Contributions from higher values of n are vanishingly small.

When a bias V_b is applied between the source and the drain, the entire system is in nonequilibrium and the chemical potential should be specified as a local chemical potential in the source μ_s, a local chemical potential in the well μ_w, and a local chemical potential in the drain μ_d. Since the two barriers are identical, we can use μ_w as the reference energy to express $\mu_s=\mu_w+V_b/2$ and $\mu_d=\mu_w-V_b/2$. When the bias V_b increases to approximately 0.1 V, μ_s moves close to the top of the GaSb valence band, resulting in a current plateau in the bias region up to about 0.15 V. With further increase of V_b, the tunneling processes occur in the energy region above the band overlap. Here, the GaSb layer works as an additional barrier and the current vanishes.

Although the shape of the *I*-*V* curve is typical for double-barrier resonant-tunneling structures, we note that in the low-bias region around $V_b=0$, there is no bias threshold and the *I*-*V* characteristics is of an Ohmic type. We will analyze this interesting phenomenon in more detail.

IV. OHMIC CONDUCTIVITY IN TUNNELING SYSTEMS

We see in Fig. 2 that the Fermi level intersects several energy levels in the magnetic-field regions around $B=1.5$, 9, and 12 T. Let E_0 be one such level and Γ_0 its level width. Since the sample specified in Fig. 1 has very thin barriers with 1.5 nm width, Γ_0 can be significantly large and comparable to the energy separation between E_0 and E_F. In this case, the Fermi energy lies in an energy region where the carrier density of states is finite, and hence the electric conductivity should be Ohmic-like. We should mention once again that using our partially self-consistent scheme, the accuracy of each energy level is within 0.25 meV. This small energy error of 0.25 meV can shift the position of each intersection very slightly but cannot remove such the intersections. Consequently, our partially self-consistent approach is accurate enough to predict the Ohmic-like electric conductivity.

To investigate this interesting phenomenon, we magnify the low-field region in Fig. 2 and reproduce it in Fig. 4. We see that at $B=2$ T, the dotted $n=0$ energy level is separated from the Fermi energy by about 0.5 meV, and the dashed

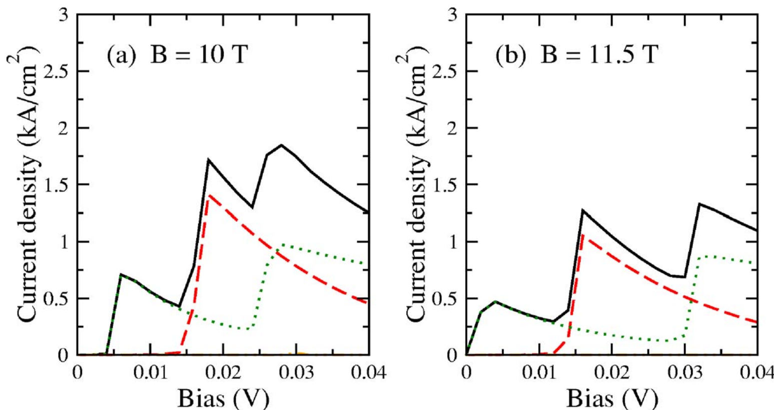

FIG. 6. (Color online) Low-bias *I*-*V* characteristics of the broken-gap structure specified in Fig. 1 for (a) $B=10$ T and (b) $B=11.5$ T.

$n=-1$ level by about 1 meV. The contributions to the current density from both these levels is of the Ohmic type as indicated in Fig. 3. At the higher field $B=2.3$ T, the energy separations increase to about 1 meV for the dotted level and about 2 meV for the dashed level. The calculated current density is plotted in Fig. 5(a). While the contributions from these two levels to the total current density is still of the Ohmic type, the dashed partial current density begins to show a deviation from the Ohmic behavior. For the case of the even higher field $B=3.5$ T, the energy difference E_0-E_F becomes larger than Γ_0 for both the dotted level and the dashed level. Hence, the current passing through each of these levels exhibits a resonant-tunneling behavior with a finite bias threshold, as shown in Fig. 5(b).

Around $B=9$ T, we see in Fig. 2 that the Fermi level intersects a dashed-dotted $n=1$ energy level. This is a *hh*-like Landau level with $\nu=3$. The electron tunneling probability through this Landau level is negligible, and, consequently, the level does not contribute to the current.

The third interesting region in Fig. 2 is around $B=12$ T. The dotted energy level is separated from E_F by about 3 meV at $B=10$ T and about 1 meV at $B=11.5$ T. Therefore, we expect a re-entry of the Ohmic conductivity when the magnetic field increases to 12 T. In Fig. 6, our calculated *I-V* curves are plotted in panel (a) for $B=10$ T and in panel (b) for $B=11.5$ T. The re-entry of the Ohmic conductivity indeed emerges going from panel (a) to panel (b).

We note that the current density in Fig. 5 is larger than that in Fig. 6. This is a consequence of the symmetry selection rule for the tunneling matrix elements. At $\mathbf{k}=0$ and zero magnetic field, tunneling of electrons from the InAs source through the *hh* states in the quantum well is forbidden by symmetry. For a finite magnetic field, the *e*-like, *lh*-like, and *hh*-like levels hybridize.[13] In this case, tunneling through a *hh*-like state is possible, and the transmission probability depends on the degree of hybridization. In Fig. 2, the dotted energy level next to the Fermi level contains a large *e*-like component at low magnetic field but a large *hh*-like component at high magnetic field. Consequently, the current density in Fig. 5 is larger than that in Fig. 6.

V. CONCLUSIONS

In this paper, we have examined how the small energy difference between a quasibound level and the Fermi level effects interband magnetotransport in a double-barrier broken-gap heterostructure. Our partially self-consistent calculation is sufficiently accurate to investigate the characteristic features of the magnetotransport through the small band-overlap energy region. The applied magnetic field can tune the *I-V* curve from a resonant-tunneling behavior to an Ohmic behavior and vice versa. To our knowledge, there has been neither theoretical prediction nor experimental evidence of this phenomenon reported in the literature. Therefore, our findings here should help to understand relevant future experiments, as well as to properly design the high-power interband cascade lasers.

[1] M. J. Yang, C. H. Yang, B. R. Bennett, and B. V. Shanabrook, Phys. Rev. Lett. **78**, 4613 (1997).
[2] R. Q. Yang, J. L. Bradshaw, J. D. Bruno, J. T. Pham, D. E. Wortman, and R. L. Tober, Appl. Phys. Lett. **81**, 397 (2002).
[3] C. L. Canedy, W. W. Bewley, J. R. Lindie, C. S. Kim, M. Kim, I. Vurgaftman, and J. R. Meyer, Appl. Phys. Lett. **88**, 161103 (2006).
[4] S. Suchalkin, M. V. Kisin, S. Luryi, G. Belenky, F. J. Towner, J. D. Bruno, C. Monroy, and R. L. Tober, Appl. Phys. Lett. **88**, 031103 (2006).
[5] M. Altarelli, Phys. Rev. B **28**, 842 (1983).
[6] G. Grosso, S. Moroni, and G. P. Parravicini, Phys. Rev. B **40**, 12328 (1989).
[7] E. Halvorsen, Y. Galperin, and K. A. Chao, Phys. Rev. B **61**, 16743 (1999).
[8] A. Zakharova, S. T. Yen, and K. A. Chao, Phys. Rev. B **64**, 235332 (2001).
[9] R. Magri, L. W. Wang, A. Zunger, I. Vurgaftman, and J. R. Meyer, Phys. Rev. B **61**, 10235 (2000).
[10] A. Zakharova, S. T. Yen, and K. A. Chao, Phys. Rev. B **66**, 085312 (2002).
[11] S. F. Tsay, J. C. Chiang, Z. M. Chau, and I. Lo, Phys. Rev. B **56**, 13242 (1997).
[12] A. Zakharova, S. T. Yen, and K. A. Chao, Phys. Rev. B **69**, 115319 (2004).
[13] K. Nilsson, A. Zakharova, I. Lapushkin, S. T. Yen, and K. A. Chao, Phys. Rev. B **74**, 075308 (2006).
[14] V. Mlinar, M. Tadić, B. Partoens, and F. M. Peeters, Phys. Rev. B **71**, 205305 (2005).
[15] I. Lapushkin, A. Zakharova, S. T. Yen, and K. A. Chao, J. Phys.: Condens. Matter **16**, 4677 (2004).
[16] J. R. Söderström, D. H. Chow, and T. C. McGill, Appl. Phys. Lett. **55**, 1094 (1989).
[17] L. F. Luo, R. Beresford, and W. I. Wang, Appl. Phys. Lett. **55**, 2023 (1989).
[18] E. E. Mendez, H. Ohno, L. Esaki, and W. I. Wang, Phys. Rev. B **43**, 5196 (1991).
[19] E. E. Mendez, Surf. Sci. **267**, 370 (1992).
[20] D. Z.-Y. Ting, E. T. Yu, and T. C. McGill, Phys. Rev. B **45**, 3583 (1992).
[21] M. S. Kiledjian, J. N. Schulman, K. L. Wang, and K. V. Rousseau, Phys. Rev. B **46**, 16012 (1992).
[22] A. Zakharova, S. T. Yen, K. Nilsson, and K. A. Chao, J. Appl. Phys. **97**, 063704 (2005).
[23] J. Genoe, K. Fobelets, C. Van Hoof, and G. Borghs, Phys. Rev. B **52**, 14025 (1995).
[24] A. Zakharova and K. A. Chao, J. Phys.: Condens. Matter **14**, 5003 (2002).
[25] A. Zakharova, K. Nilsson, K. A. Chao, and S. T. Yen, Phys. Rev. B **72**, 115329 (2005).
[26] Y. X. Liu, R. R. Marquardt, D. Z.-Y. Ting, and T. C. McGill, Phys. Rev. B **55**, 7073 (1997).

[27] A. Zakharova, I. Lapushkin, S. T. Yen, K. Nilsson, and K. A. Chao, *Recent Research Development in Science and Technology of Semiconductors* (Transworld Research Network, Kerala, 2004), Vol. 2, pp. 37-72.
[28] David Yuk Kei Ko and J. C. Inkson, Phys. Rev. B **38**, 9945 (1988).
[29] B. A. Foreman, Phys. Rev. B **56**, R12748 (1997).
[30] D. J. Barnes, R. J. Nicholas, R. J. Warburton, N. J. Mason, P. J. Walker, and N. Miura, Phys. Rev. B **49**, 10474 (1994).
[31] I. Lapushkin, A. Zakharova, V. Gergel, H. Goronkin, and S. Tehrani, J. Appl. Phys. **82**, 2421 (1997).
[32] G. Y. Wu, T. C. McGill, C. Mailhiot, and D. L. Smith, Phys. Rev. B **39**, 6060 (1989).
[33] M. P. C. M. Krijn, Semicond. Sci. Technol. **6**, 27 (1991).